Bimodal Phase Diagram of the Superfluid Density in $LaAlO_3/SrTiO_3$ Revealed by an Interfacial Waveguide Resonator

Nicola Manca,[1,*] Daniel Bothner,[1] Ana M. R. V. L. Monteiro,[1] Dejan Davidovikj,[1] Yildiz G. Sağlam,[1] Mark Jenkins,[1] Marc Gabay,[2] Gary A. Steele,[1] and Andrea D. Caviglia[1]

[1]*Kavli Institute of Nanoscience, Delft University of Technology, P.O. Box 5046, 2600 GA Delft, Netherlands*

[2]*Laboratoire de Physique des Solides, Universite Paris-Sud and CNRS, Batiment 510, 91450 Orsay, France*

(Received 1 October 2018; published 24 January 2019)

We explore the superconducting phase diagram of the two-dimensional electron system at the $LaAlO_3/SrTiO_3$ interface by monitoring the frequencies of the cavity modes of a coplanar waveguide resonator fabricated in the interface itself. We determine the phase diagram of the superconducting transition as a function of the temperature and electrostatic gating, finding that both the superfluid density and the transition temperature follow a dome shape but that the two are not monotonically related. The ground state of this two-dimensional electron system is interpreted as a Josephson junction array, where a transition from long- to short-range order occurs as a function of the electronic doping. The synergy between correlated oxides and superconducting circuits is revealed to be a promising route to investigate these exotic compounds, complementary to standard magnetotransport measurements.

DOI: 10.1103/PhysRevLett.122.036801

The interface between the two wide band-gap insulators $LaAlO_3$ (LAO) and $SrTiO_3$ (STO) hosts a two-dimensional electron system (2DES) [1,2] that shows superconductivity [3] together with strong spin-orbit coupling [4,5], localized magnetic moments [6,7], and long-range spin coherence [8]. Its low carrier concentration makes this 2DES particularly sensitive to electrostatic gating, and a superconductor-insulator transition, tunable Rashba splitting, and tunable superconductivity have already been demonstrated [9–11]. Despite being considered the prototypical correlated 2DES and a platform to realize tunable superconducting devices [12–14], the nature of its superconducting ground state and dome-shaped phase diagram, observed upon electrostatic doping, is still not understood. This partly stems from the fact that standard magnetotransport measurements do not allow us to directly probe the superfluid density, and so far few approaches have been proposed to overcome such a limitation. Bert *et al.* employed a scanning-SQUID technique to measure the penetration depth of the screening supercurrents and extract the superfluid density of the 2DES [15], while, more recently, Singh *et al.* calculated the variations of the superfluid density from the resonance frequency of a RLC circuit containing a lumped LAO/STO element by means of an equivalent-circuit model [16]. A powerful tool to probe the superfluid density are the superconducting coplanar waveguide resonators (SCWRs). SCWRs are cavities for the electromagnetic field, where the frequencies of the standing waves are determined by the interplay between the geometry and electromagnetic environment [17–19]. The formation of quasiparticles in a SCWR causes a downshift of their resonance frequencies, because the lower superfluid density increases the kinetic inductance [20,21]. The high sensitivity of such devices warranted their integration in highly demanding applications, such as quantum technologies [22–24] and astronomy [25,26].

Here, we realize a SCWR by direct patterning of the 2DES at the LAO/STO interface. This approach gives a stronger modulation of the resonance frequency in comparison to lumped-element designs used in previous implementations. The resonance frequencies of the SCWR cavity modes are monitored as a function of the temperature and electrostatic doping and translated into variations of the Pearl length and superfluid density. We find that both the critical temperature and superfluid density display a dome-like shape as a function of the back-gate voltage, which are not monotonically related. This nonmonotonic behavior arises from the ground state of the system, which is identified as a Josephson junction array shifting from short- to long-range order while driving the system from the under- to the overdoped condition.

The pristine heterostructure is obtained by the pulsed laser deposition of 12 unit cells of crystalline LAO on top of a TiO_2-terminated $SrTiO_3(100)$ substrate. As sketched in Fig. 1(a), by means of electron beam lithography and ion milling, we separate the central line from the ground plane (GND). The line has a width W of 40 μm, a nominal length l of 2.5 mm, and a spacing S of 10 μm from the GND. Details of the fabrication are reported in Supplemental Material, Sec. 1 [27]. One end of the SCWR is isolated from the GND, while the other is wire bonded to the feed line. The large impedance mismatch at the two ends of the

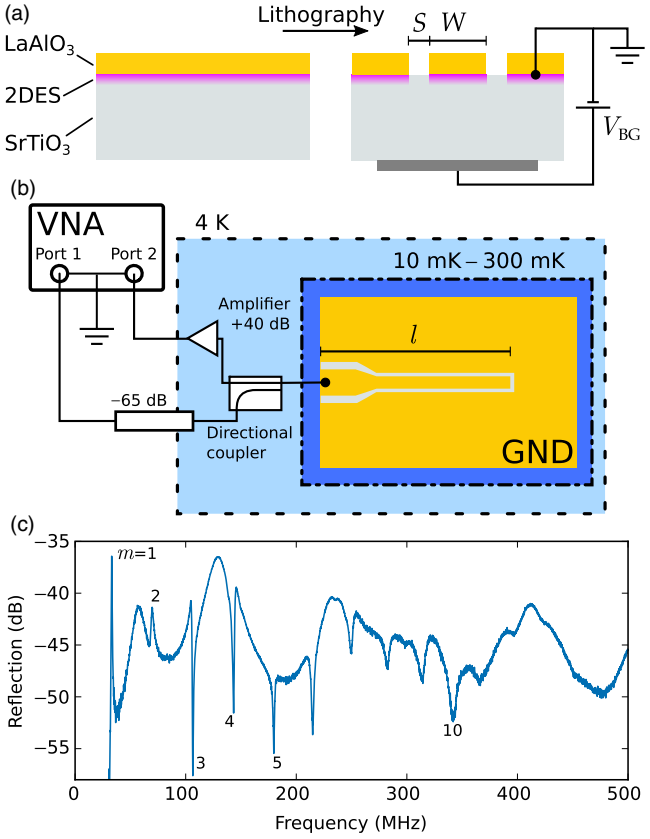

FIG. 1. A coplanar waveguide resonator at the LAO/STO interface. (a) Sketch of the 2DES (magenta) at the LAO/STO (yellow/gray) interface before (left) and after (right) the lithography. The field effect is obtained by tuning the voltage (V_{BG}) of the back gate. (b) Experimental setup to probe the SCWR. The −65 dBm attenuation is distributed across the stages from room temperature to the mK plate. (c) Reflection spectrum of the SCWR measured at 11 mK, $V_{BG} = 0$ V, and −95 dBm.

line realizes a nearly half-wavelength ($\lambda/2$) resonator. The cavity modes of the SCWR are measured with a vector network analyzer (VNA), as indicated in Fig. 1(b). The power of the signal injected into the SCWR is about −95 dBm. The sample is glued to an isolated holder with conductive silver paint, which enables field effect measurements in the back-gate geometry. The GND and the line share the same electrical ground, so the back-gate voltage (V_{BG}) affects both. Figure 1(c) shows the response spectrum of the SCWR at $T = 11$ mK and $V_{BG} = 0$ V. More than ten modes can be identified on top of an oscillating background, which stems from interference in the connecting circuitry. We based our analysis on the modes from $m = 2$ to $m = 5$, because $m = 1$ is at the edge of the cutoff frequency of the amplifier (30 MHz) [cf. Fig. 1(b)], and the higher modes show lower visibility in the explored space of parameters. The mode visibility as a function of the temperature and V_{BG} is determined by the proximity to the critical coupling condition and by the damping coming from different sources of losses, with coupling, quasiparticles, and dielectric losses being the major ones. Here, the broadening and weakening of the peaks at higher frequencies are in agreement with what is expected from the $SrTiO_3$ substrate [28].

An open-end half-wavelength resonator excited at the eigenfrequency f_m can be modeled as a parallel RLC circuit with the resonance frequency $f_m = 1/(2\pi\sqrt{L_m C})$, where the inductance L_m is mode dependent [29]. In general, the inductance of a superconducting resonator is given by both a geometric and a kinetic contribution [30]. In our SCWR, already the first mode has a total geometric inductance of about 0.16 nH, while the kinetic inductance at $T = 11$ mK (the lowest value) is about 4 nH. L_m is thus dominated by the kinetic contribution, similarly to what has been observed in other LAO/STO superconducting devices [13,31]. This allows us to write the two simple following expressions for the Pearl length Λ and the 2D superfluid density n:

$$\Lambda = \alpha(m/f_m)^2, \tag{1}$$

$$n = \beta(f_m/m)^2, \tag{2}$$

where α and β are determined by the line geometry, the dielectric environment, and the effective mass of the charge carriers, as discussed in Supplemental Material, Sec. 2 [27]. By monitoring the magnitude of f_m as a function of T and V_{BG}, it is thus possible to investigate their effect on the superconducting state of the 2DES. The high sensitivity of this probing technique is due to the low density of Cooper pairs and the consequent high kinetic inductance of the 2DES. However, we note that the calculated values of the n suffer from two main sources of error. First, the two ends of the line are not perfect mirrors, and the values of f_m are thus influenced by both the geometry of the launcher and the capacitance of the bonding pad. Second, the size of the bonding wires connecting the line leads to an estimation of its effective length of 2.38 ± 0.12 mm (see Supplemental Material, Sec. 1 [27]). We thus consider a confidence interval of $\pm 10\%$ for the calculated absolute values of n and Λ.

Figure 2(a) shows the temperature dependence of the cavity modes of the SCWR from $m = 2$ to $m = 5$ at $V_{BG} = 0$ V. All the modes are evenly spaced, and their relative variations are in good agreement. The disappearance of the cavity modes above 120 mK comes from the increased power dissipation associated with the formation of quasiparticles while approaching the superconducting transition. In the normal state, this device shows no resonance peaks, owing to the high resistivity of the metallic LAO/STO. From Eqs. (1) and (2), it is possible to extract the temperature dependence of Λ and n from the frequencies of each cavity mode. The calculated values are plotted in Figs. 2(b) and 2(c), respectively. At the base

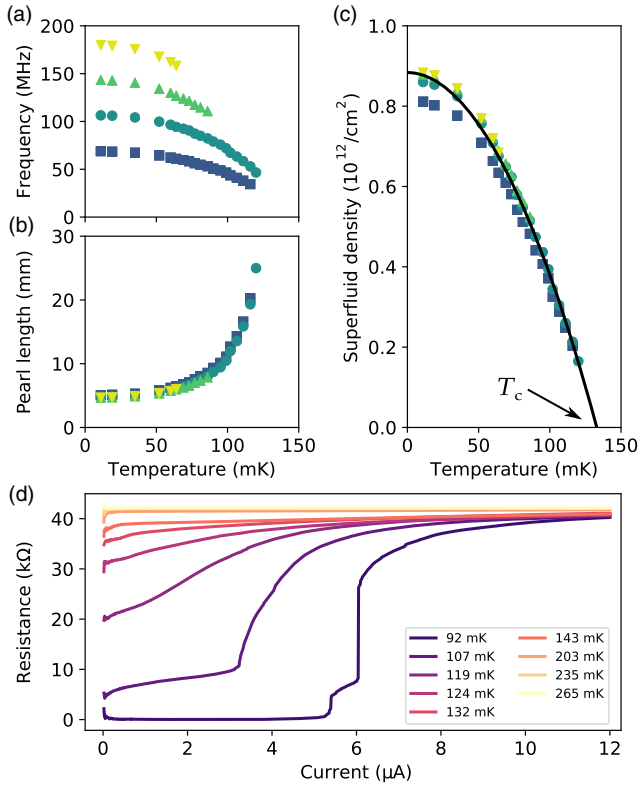

FIG. 2. Temperature dependence of the superfluid characteristics. (a) Frequencies of the cavity modes from $m = 2$ (blue squares) to $m = 5$ (yellow reversed triangles) at $V_{BG} = 0$ V. (b) Pearl length and (c) superfluid density calculated from the data in (a) using Eqs. (1) and (2). The solid line in (c) is the best fit of Eq. (3) for $m = 3$, which gives $T_c = 133 \pm 2$ mK. (d) Resistance-current characteristics measured on the ground plane.

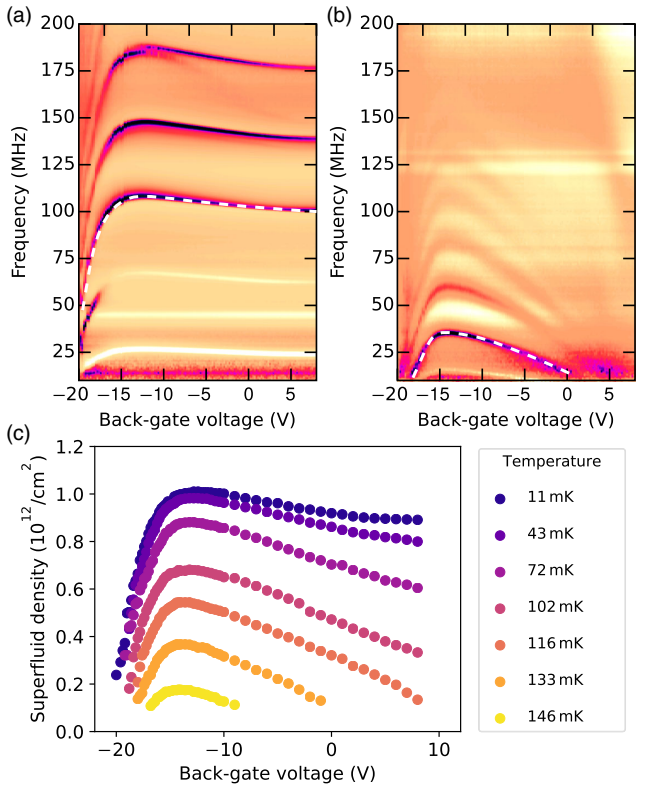

FIG. 3. Superfluid density under the field effect. (a),(b) Reflection amplitude of the SCWR as a function of V_{BG} at (a) 11 and (b) 133 mK. The white dashed line is a guide to the eye highlighting $m = 3$. (c) Temperature-back-gate phase diagram of the superfluid density calculated from $m = 3$.

temperature, we have $\Lambda(11\ \mathrm{mK}) = 4.8 \pm 0.5$ mm, in good agreement with what was estimated in Ref. [13], that increases to above 23 mm at 120 mK. An opposite trend is observed for n, which starts from 0.87×10^{12} cm^{-2} at 11 mK with a negative slope that becomes progressively more pronounced. We fit the temperature dependence of n with a phenomenological BCS model

$$n = n_0\left[1 - \left(\frac{T}{T_c}\right)^{\gamma}\right], \tag{3}$$

where n_0 is the zero-temperature superfluid density, T_c is the superconducting critical temperature, and γ is an exponent which describes the opening of the gap below T_c [15,32]. The black solid line in Fig. 2(c) is the best fit of Eq. (3) calculated for the third mode (circles in Fig. 2). If we consider both the second and third modes, which show the best visibility in temperature, we obtain $\gamma = 1.95 \pm 0.23$ and $\gamma = 1.96 \pm 0.20$, respectively. These results are in fairly good agreement with a clean s-wave BCS scenario, where a value of $\gamma = 2$ is predicted [32]. This is in contrast with previous works reporting $\gamma = 2.8$ [15] and a possible indication of lower disorder in our sample [33]. The calculated critical temperature is $T_c = 133$ mK, that we can compare with the transport measurements in Fig. 2(d) performed by wire bonding the ground plane (see also Supplemental Material, Sec. 2 [27]). The electrical resistance is current dependent below 132 mK, and a sharp transition is observed below 119 mK. Although a quantitative analysis is not possible because of the inhomogeneous current flow, we can consider the T_c as the temperature at which the electrical resistance at zero bias reaches half of its normal state, obtaining ≈120 mK, in good agreement with the temperature dependence of the SCWR cavity modes.

Our experimental configuration enables tuning the superfluid density of the 2DES by the electric-field effect. In Figs. 3(a) and 3(b), we show two color maps of the spectral response of the SCWR measured at 11 and 133 mK as a function of V_{BG}. At the base temperature, when the gate voltage goes below −20 V, the cavity modes rapidly shift to low frequencies and then disappear, while at positive voltages the response is rather flat with a slightly decreasing trend. At 133 mK, instead, the superconductivity can be quenched on both ends of the phase diagram with all the modes showing a pronounced domelike

response. This response originates from the modulation of n, and a possible contribution to the observed signal from the electric-field dependence of the STO dielectric constant [28,34,35] is discussed and ruled out in Supplemental Material, Sec. 4 [27]. Similarly to the analysis reported in Fig. 2, we calculate the voltage dependence of n at different temperatures using Eq. (2). Here, we base our analysis on the third mode ($m = 3$), which shows the best visibility over the whole space of parameters, while a complete dataset of the first five modes is reported in Supplemental Material, Sec. 5 [27]. The phase diagram of the superfluid density reported in Fig. 3(c) is characterized by a domelike shape that becomes progressively lower and narrower for increasing temperatures. It peaks at about -12.5 V, where superconductivity is still detected at 146 mK, well above $T_c = 132$ mK calculated from Fig. 2(c) and indicating that the pristine 2DES is in the overdoped regime. The maximum value of the Cooper pair density is $n \approx 1 \times 10^{12}$ cm^{-2}, corresponding to an electron density of 2×10^{12} cm^{-2}. This is in agreement with previous experiments [15,16,36,37], supporting the conclusion that only a small fraction of charge carriers participate in the superconductivity.

In Fig. 4(a), we compare the effect of V_{BG} on n at the base temperature and T_c, where the latter was calculated by fitting the data reported in Fig. 3 with Eq. (3). Both of them display a well-defined dome-shape dependence, with a maximum at $V_{\mathrm{BG}} \approx -12.5$ V. The different position of their maximal value comes from a progressive shift of the maximum of $n(V_{\mathrm{BG}})$ with the temperature and is discussed in Supplemental Material, Sec. 6 [27]. Different explanations have been proposed for this peculiar phase diagram. The peak of the T_c has been ascribed to the Lifshitz transition, where the overdoped regime is a consequence of the onset of population of d_{xz}, d_{yz} bands [36], to low-density carriers located in a high-mobility band showing a nonmonotonic population under the field effect due to the interplay of orbital effects and correlations [37], or to a combination between the multiband nature of this 2DES, electronic correlations, and disorder [16,38]. The interplay between $n(11\ \mathrm{mK})$ and T_c can be further investigated considering the $T_c - n(11\ \mathrm{mK})$ plot in Fig. 4(b). An upper and lower branch appear, corresponding to the over- and underdoped condition, respectively, and connected at $V_{\mathrm{BG}} \approx -12$ V (optimal doping). A similar bimodal distribution was also reported by Bert *et al.* (gray dataset of Fig. 3 in Ref. [15]) and ascribed to inhomogeneities that locally suppress n in the overdoped regime. In our case, this interpretation is at variance with the results from Fig. 2(c), where the critical exponent $\gamma \approx 2$ indicates low disorder.

The data presented in this work allow one to view the superconducting phase as the ground state of a Josephson junction array. For zero gate voltage, Fig. 2(d) shows that increasing the current I in the device produces dissipation

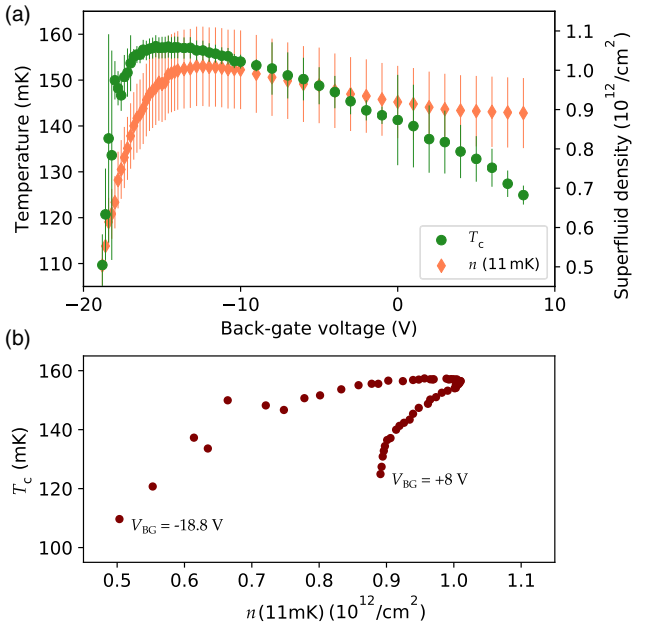

FIG. 4. Analysis of the superfluid gate dependence. (a) T_c and $n(11\ \mathrm{mK})$ as a function of V_{BG}. T_c is calculated by fitting the data from Fig. 3(c) with Eq. (3). (b) Critical temperature as a function of the superfluid density at 11 mK.

above a temperature-dependent threshold. Upon a further increase of I, one observes a steep rise in the resistance R beyond a second threshold, and R ultimately levels off to its normal state value. In the Josephson junction language, a BKT-like (Berezinsky-Kosterlitz-Thouless) transition takes place at the lower threshold value $I_{c1} = E_J/(\varepsilon_v \Phi_0)$, where I_{c1} represents the typical maximum supercurrent of a junction, E_J is the Josephson coupling, and $\Phi_0 = h/(2e)$ is the flux quantum [39]. The dielectric constant ε_v jumps from a finite value to infinity at the transition (strictly speaking, this holds only at $T = 0$), and dissipation sets in above I_{c1}. For still larger values of the current, individual junctions in the array can sustain phase coherence (short-range order) as long as $I < I_{c2} = E_J/\Phi_0$. For $I > I_{c2}$, the array eventually crosses over to the normal state. In the intermediate regime $I_{c1} < I < I_{c2}$, one may then define a bare (unrenormalized) density of Cooper pairs n_0 [39] such that

$$n_0 = \frac{2m_e}{2\pi\hbar^2} I_{c2} \Phi_0. \tag{4}$$

From Fig. 2(d), we determine $\{[I_{c2}(92\,\mathrm{mK})]/[I_{c2}(109\,\mathrm{mK})]\} = 1.8$. This number is in line with the ratio that one can extract from the temperature dependence of the cavity modes in Fig. 2(c), which is $\{[n_0(92\ \mathrm{mK})]/[n_0(109\ \mathrm{mK})]\} = 1.79$. From Fig. 2(d), we see that for increasing temperatures I_{c1} and I_{c2} are no longer distinguishable, and T_c goes to zero together with n. The temperature dependence of n reported in Fig. 2(c)

(overdoped condition) can be thus interpreted as a regime where the superconducting islands are large enough to sustain long-range coherence and $n(T)$ follows the simple BCS model of Eq. (3), that in this case was found compatible with a clean s-wave superconductor. In the underdoped condition, the lowered electron density makes the superconducting puddles lose the connection, resulting in a transition dominated by short-range order. This picture explains the two branches in Fig. 4(b), originating from the different nature of the ground state in the two regimes, in agreement with recent experimental results [40,41]. We may now justify the fact that transport properties of the 2DES in this device can be related to their counterpart in Josephson junction networks. In Fig. 2(d), the steep rise in the resistance at $T = 92$ mK is observed at $I_{c1}(92\ \mathrm{mK}) = 5.4\ \mu\mathrm{A}$. The equations leading to Eq. (4) also predict that the value of the critical current per junction is $I_{c2}(92\ \mathrm{mK}) \approx 37$ nA and $I_{c2}(109\ \mathrm{mK}) \approx 20$ nA, suggesting that about 150 parallel channels are contributing to the electrical current.

Below $T = 105$ K, STO undergoes a structural transition from a cubic to a tetragonal phase [42,43]. Current maps of the charge flow in LAO/STO reveal a filamentary structure of the pattern which is related to the striped electrostatic potential modulation arising from the tetragonal domains in STO at a low temperature [44–48]. However, the spatial resolution is not sufficient to simultaneously image the current paths and the domain boundaries; the size of the latter does not exceed 500–600 nm. Estimations of the wall (twins, dislocations) widths in the bundles reported by several authors are between a few tens of nanometers [45,46] and 1–10 nm [49,50]. If the conducting channel consists of a bundle of filaments of micrometer size, one could consider each filament as forming a junction neighboring filaments being separated by 10 nm walls. By considering about 150 parallel junctions, one recovers an approximate size of a few microns for the bundle.

In conclusion, we studied the superfluid density at the LAO/STO interface by means of a coplanar waveguide resonator patterned into the heterostructure itself. With no gate applied, the temperature dependence of the superfluid density is in good agreement with a clean s-wave BCS superconductor, while under the field effect both the critical temperature and the superfluid density show a dome-shaped phase diagram, leading to a multivalued relationship between them. The comparison between the transport data and cavity resonances suggests that the ground state of this 2DES is a Josephson junction array undergoing a transition between long- and short-range order under electrostatic doping. We foresee future experiments taking advantage of the high sensitivity of this technique, as an example by combining superconducting resonators and magnetotransport measurements to explore different oxide-based 2DES.

The numerical data shown in figures of the manuscript and the supplemental material can be downloaded from the Zenodo online repository [51].

The research leading to these results has received funding from the European Research Council under the European Union's H2020 program/ERC Grant Agreement No. 677458, the project Quantox of QuantERA ERA-NET Cofund in Quantum Technologies, the Netherlands Organisation for Scientific Research (NWO/OCW) as part of the Frontiers of Nanoscience program (NanoFront), and by the Dutch Foundation for Fundamental Research on Matter (FOM).

*manca@fisica.unige.it

[1] A. Ohtomo and H. Y. Hwang, Nature (London) **427**, 423 (2004).
[2] C. Cen, S. Thiel, J. Mannhart, and J. Levy, Science **323**, 1026 (2009).
[3] N. Reyren, S. Thiel, A. D. Caviglia, L. Fitting Kourkoutis, G. Hammerl, C. Richter, C. W. Schneider, T. Kopp, A.-S. Rüetschi, D. Jaccard, M. Gabay, D. A. Muller, J.-M. Triscone, and J. Mannhart, Science **317**, 1196 (2007).
[4] M. Ben Shalom, M. Sachs, D. Rakhmilevitch, A. Palevski, and Y. Dagan, Phys. Rev. Lett. **104**, 126802 (2010).
[5] M. Diez, A. M. R. V. L. Monteiro, G. Mattoni, E. Cobanera, T. Hyart, E. Mulazimoglu, N. Bovenzi, C. W. J. Beenakker, and A. D. Caviglia, Phys. Rev. Lett. **115**, 016803 (2015).
[6] J. A. Bert, B. Kalisky, C. Bell, M. Kim, Y. Hikita, H. Y. Hwang, and K. a. Moler, Nat. Phys. **7**, 767 (2011).
[7] L. Li, C. Richter, J. Mannhart, and R. C. Ashoori, Nat. Phys. **7**, 762 (2011).
[8] R. Ohshima, Y. Ando, K. Matsuzaki, T. Susaki, M. Weiler, S. Klingler, H. Huebl, E. Shikoh, T. Shinjo, S. T. B. Goennenwein, and M. Shiraishi, Nat. Mater. **16**, 609 (2017).
[9] A. D. Caviglia, S. Gariglio, N. Reyren, D. Jaccard, T. Schneider, M. Gabay, S. Thiel, G. Hammerl, J. Mannhart, and J.-M. Triscone, Nature (London) **456**, 624 (2008).
[10] C. Bell, S. Harashima, Y. Kozuka, M. Kim, B. G. Kim, Y. Hikita, and H. Y. Hwang, Phys. Rev. Lett. **103**, 226802 (2009).
[11] A. D. Caviglia, M. Gabay, S. Gariglio, N. Reyren, C. Cancellieri, and J.-M. Triscone, Phys. Rev. Lett. **104**, 126803 (2010).
[12] A. M. R. V. L. Monteiro, D. J. Groenendijk, N. Manca, E. Mulazimoglu, S. Goswami, Y. Blanter, L. M. K. Vandersypen, and A. D. Caviglia, Nano Lett. **17**, 715 (2017).
[13] S. Goswami, E. Mulazimoglu, A. M. R. V. L. Monteiro, R. Wölbing, D. Koelle, R. Kleiner, Y. M. Blanter, L. M. K. Vandersypen, and A. D. Caviglia, Nat. Nanotechnol. **11**, 861 (2016).
[14] H. Thierschmann, E. Mulazimoglu, N. Manca, S. Goswami, T. M. Klapwijk, and A. D. Caviglia, Nat. Commun. **9**, 2276 (2018).
[15] J. A. Bert, K. C. Nowack, B. Kalisky, H. Noad, J. R. Kirtley, C. Bell, H. K. Sato, M. Hosoda, Y. Hikita, H. Y. Hwang, and K. A. Moler, Phys. Rev. B **86**, 060503 (2012).

[16] G. Singh, A. Jouan, L. Benfatto, F. Couëdo, P. Kumar, A. Dogra, R. C. Budhani, S. Caprara, M. Grilli, E. Lesne, A. Barthélémy, M. Bibes, C. Feuillet-Palma, J. Lesueur, and N. Bergeal, Nat. Commun. **9**, 407 (2018).

[17] M. J. Lancaster, J. Powell, and A. Porch, Supercond. Sci. Technol. **11**, 1323 (1998).

[18] M. P. J. Tiggelman, K. Reimann, F. Van Rijs, J. Schmitz, and R. J. E. Hueting, IEEE Trans. Electron Devices **56**, 2128 (2009).

[19] A. Ahmed, I. A. Goldthorpe, and A. K. Khandani, Appl. Phys. Rev. **2**, 011302 (2015).

[20] J. Baselmans, S. Yates, P. de Korte, H. Hoevers, R. Barends, J. Hovenier, J. Gao, and T. Klapwijk, Adv. Space Res. **40**, 708 (2007).

[21] N. Vercruyssen, R. Barends, T. M. Klapwijk, J. T. Muhonen, M. Meschke, and J. P. Pekola, Appl. Phys. Lett. **99**, 062509 (2011).

[22] P. Nataf and C. Ciuti, Phys. Rev. Lett. **107**, 190402 (2011).

[23] Z.-L. Xiang, S. Ashhab, J. Q. You, and F. Nori, Rev. Mod. Phys. **85**, 623 (2013).

[24] J. M. Chow, J. M. Gambetta, E. Magesan, D. W. Abraham, A. W. Cross, B. R. Johnson, N. A. Masluk, C. A. Ryan, J. A. Smolin, S. J. Srinivasan, and M. Steffen, Nat. Commun. **5**, 4015 (2014).

[25] J. Baselmans, S. J. C. Yates, R. Barends, Y. J. Y. Lankwarden, J. R. Gao, H. Hoevers, and T. M. Klapwijk, J. Low Temp. Phys. **151**, 524 (2008).

[26] J. Bueno, O. Yurduseven, S. J. C. Yates, N. Llombart, V. Murugesan, D. J. Thoen, A. M. Baryshev, A. Neto, and J. J. A. Baselmans, Appl. Phys. Lett. **110**, 233503 (2017).

[27] See Supplemental Material at http://link.aps.org/supplemental/10.1103/PhysRevLett.122.036801 for device fabrication, calculation of Λ and n from the f_m, DC V–I measurements, contribution of the dielectric constant of $SrTiO_3$ to the measured frequency shift, the first five cavity modes as a function of T and V_{BG}, and the temperature dependence of the optimal doping condition.

[28] D. Davidovikj, N. Manca, H. S. J. van der Zant, A. D. Caviglia, and G. A. Steele, Phys. Rev. B **95**, 214513 (2017).

[29] M. Göppl, A. Fragner, M. Baur, R. Bianchetti, S. Filipp, J. M. Fink, P. J. Leek, G. Puebla, L. Steffen, and A. Wallraff, J. Appl. Phys. **104**, 113904 (2008).

[30] K. Watanabe, K. Yoshida, T. Aoki, and S. Kohjiro, Jpn. J. Appl. Phys. **33**, 5708 (1994).

[31] O. Copie, V. Garcia, C. Bodefeld, C. Carrétéro, M. Bibes, G. Herranz, E. Jacquet, J.-L. Maurice, B. Vinter, S. Fusil, K. Bouzehouane, H. Jaffrès, and A. Barthélémy, Phys. Rev. Lett. **102**, 216804 (2009).

[32] R. Prozorov and R. W. Giannetta, Supercond. Sci. Technol. **19**, R41 (2006).

[33] J. P. Carbotte, Rev. Mod. Phys. **62**, 1027 (1990).

[34] R. C. Neville, B. Hoeneisen, and C. A. Mead, J. Appl. Phys. **43**, 2124 (1972);

[35] J. Hemberger, P. Lunkenheimer, R. Viana, R. Böhmer, and A. Loidl, Phys. Rev. B **52**, 13159 (1995).

[36] A. Joshua, S. Pecker, J. Ruhman, E. Altman, and S. Ilani, Nat. Commun. **3**, 1129 (2012).

[37] E. Maniv, M. Ben Shalom, A. Ron, M. Mograbi, A. Palevski, M. Goldstein, and Y. Dagan, Nat. Commun. **6**, 8239 (2015).

[38] T. V. Trevisan, M. Schütt, and R. M. Fernandes, Phys. Rev. Lett. **121**, 127002 (2018).

[39] C. J. Lobb, D. W. Abraham, and M. Tinkham, Phys. Rev. B **27**, 150 (1983).

[40] J. Biscaras, N. Bergeal, S. Hurand, C. Feuillet-Palma, A. Rastogi, R. C. Budhani, M. Grilli, S. Caprara, and J. Lesueur, Nat. Mater. **12**, 542 (2013).

[41] Z. Chen, A. G. Swartz, H. Yoon, H. Inoue, T. Merz, D. Lu, Y. Xie, H. Yuan, Y. Hikita, S. Raghu, and H. Y. Hwang, Nat. Commun. **9**, 4008 (2018).

[42] H. Unoki and T. Sakudo, J. Phys. Soc. Jpn. **23**, 546 (1967).

[43] D. Roy, Y. Frenkel, S. Davidovitch, E. Persky, N. Haham, M. Gabay, B. Kalisky, and L. Klein, Phys. Rev. B **95**, 245303 (2017).

[44] Y. Frenkel, N. Haham, Y. Shperber, C. Bell, Y. Xie, Z. Chen, Y. Hikita, H. Y. Hwang, and B. Kalisky, ACS Appl. Mater. Interfaces **8**, 12514 (2016).

[45] Y. Frenkel, N. Haham, Y. Shperber, C. Bell, Y. Xie, Z. Chen, Y. Hikita, H. Y. Hwang, E. K. Salje, and B. Kalisky, Nat. Mater. **16**, 1203 (2017).

[46] M. Honig, J. A. Sulpizio, J. Drori, A. Joshua, E. Zeldov, and S. Ilani, Nat. Mater. **12**, 1112 (2013).

[47] H. Noad, P. Wittlich, J. Mannhart, and K. A. Moler, arXiv:1805.08549.

[48] Y.-Y. Pai, H. Lee, J.-W. Lee, A. Annadi, G. Cheng, S. Lu, M. Tomczyk, M. Huang, C.-B. Eom, P. Irvin, and J. Levy, Phys. Rev. Lett. **120**, 147001 (2018).

[49] K. Szot, W. Speier, G. Bihlmayer, and R. Waser, Nat. Mater. **5**, 312 (2006).

[50] A. Schiaffino and M. Stengel, Phys. Rev. Lett. **119**, 137601 (2017).

[51] N. Manca, D. Bothner, A. M. R. V. L. Monteiro, D. Davidovikj, Y. G. Sağlam, M. Jenkins, M. Gabay, G. Steele, and A. D. Caviglia, Zenodo DOI: 10.5281/zenodo.2530003 (2019)